Radar-Based Human Motion Recognition by Using Vital Signs with ECA-CNN

Kaiyu CHEN, Minming GU, Zhixiang CHEN

School of Information Science and Engineering, Zhejiang Sci-Tech University, No.2 Street 928, 310018 Hangzhou, China

guminming@zstu.edu.cn

Abstract. *Radar technologies reserve a large latent capacity in dealing with human motion recognition (HMR). For the problem that it is challenging to quickly and accurately classify various complex motions, an HMR algorithm combining the attention mechanism and convolution neural network (ECA-CNN) using vital signs is proposed. Firstly, the original radar signal is obtained from human chest wall displacement. Chirp-Z Transform (CZT) algorithm is adopted to refine and amplify the narrow band spectrum region of interest in the global spectrum of the signal, and accurate information on the specific band is extracted. Secondly, six time-domain features were extracted for the neural network. Finally, an ECA-CNN is designed to improve classification accuracy, with a small size, fast speed, and high accuracy of 98%. This method can improve the classification accuracy and efficiency of the network to a large extent. Besides, the size of this network is 100 kb, which is convenient to integrate into the embedded devices.*

Keywords

Human motion recognition, vital signs, Efficient Channel Attention enabled Convolutional Neural Network (ECA-CNN), radar

1. Introduction

The population of the older aged over 60 years has increased dramatically [1]. It is reported that the ratio of this age range will reach 17% in the world by 2050. Due to the large population [2], in-home health monitoring [3], [4] has become the focus of many research. Among them, human motion detection is one of the critical technologies. Human motion can be detected by many devices, such as wearable sensors [5], [6], wireless sensor devices [7], depth cameras [8], and radar equipment [9–11]. While wearable sensors are usually attached to a person they are inconvenient in terms of user experience. The cameras with intelligent methods always have a high recognition accuracy but perform poorly in protecting privacy. Since the radar is contactless, privacy-preserving, and does not need a strict installation requirement, it has become an ideal human motion recognition device.

Ultra-wideband (UWB) radar [12], [13], continuous wave (CW) radar [14], [15], and frequency-modulated continuous wave (FMCW) radar [16–18] are most commonly used in in-home monitoring. In [19], the authors integrate a multiclass classification structure into the human motion recognition algorithm. Based on this structure, they classify the specific in-situ and non-in-situ motion through different features. Compared with CW radar, FMCW radar can obtain both the speed and position information of humans. Furthermore, FMCW radar avoids peak-to-average power ratio in transmission and simplifies the design process of the power amplifier and RF components that are not available for UWB radar [20], [21]. Therefore, this paper adopts FMCW radar for human non-contact motion recognition.

In the field of FMCW radar research [22], the non-contact detection of human vital signs [23] and motions has emerged in the last decade. In vital sign detection, various researchers have contributed to detecting respiration and heart rate, two essential vital signs that indicate the basic functioning of the human body. Lee et al. use a 24-GHz FMCW radar for heartbeat rate estimation, and they eliminate the environment clutter noise and reduce the mutual interference among multiple people [24]. In [25], the authors apply a 7.3-GHz FMCW radar for heartbeat and respiration rate detection. To reduce the influence of the indoor environment on vital sign estimation, Marco et al. propose a multipath propagation model for heartbeat rate and respiration rate detection. People have successfully solved the problems of environmental noise [26], [27], multi-person detection [28], [29], and movement interference [30], [31] in vital sign detection. Furthermore, in motion identification, HMR developed rapidly in methods and recognition accuracy at present. For instance, Vandersmissen et al. investigate micro-Doppler features from gait to classify five indoor persons with an error rate of 21.54% [17]; Kim uses CW radar to extract Doppler features and uses a DCNN to identify seven human movements [32]. The accuracy of classification results is 90.9%. In the human motion recognition algorithm, a multidimensional principal component analysis (MPCA) method [33] combined with Doppler-range information is proposed. Combined with phase information, the instantaneous velocity and acceleration of the human body are obtained for action detection. Bryan et al. apply the PCA method to feature extraction based on UWB radar and clas-

sified eight kinds of human motions [34]. The recognition accuracy reached more than 85%.

However, most studies focused on motion recognition using the time-range map, time-Doppler map, and time-range-Doppler map, which are challenging to integrated devices of human motion recognition for it contains only data information.

Therefore, this article proposes a human motion detection and recognition method for five human motions using an FMCW radar. Specifically, the raw radar motion data is used to obtain the intermediate frequency (IF) signal and acquire the human breath and heartbeat signals. Original chest wall displacement acquired by radar is processed with the CZT algorithm and gets respiratory and heart rate signals. Then, normalizing the sign spectrum, features such as amplitude, slope, and zero-crossing time are extracted. Besides, an ECA-CNN network based on feature extraction is designed to classify different human actions.

The framework of this paper is illustrated in Fig. 1. The FMCW radar signal processing is described in Sec. 2, including the human motion detection feature extraction and ECA-CNN. The experimental results and corresponding analysis are presented in Sec. 3. In the end, the conclusion and outlook are drawn in Sec. 4.
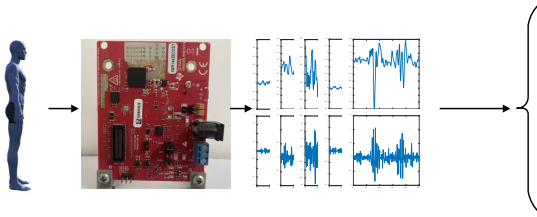
Fig. 1. The system block diagram for identifying five actions with radar data.
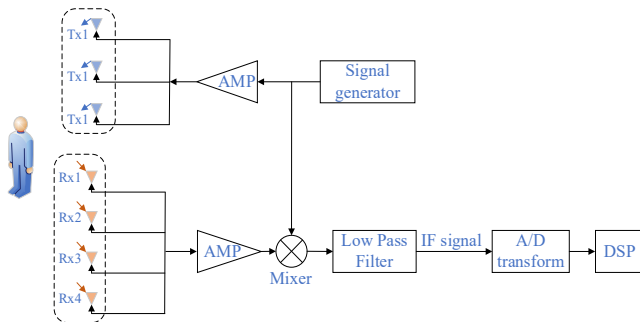
Fig. 2. Block diagram of the FMCW radar system.

2. Methods

2.1 FMCW Radar Signal Processing

FMCW radar is used to collect respiratory and heartbeat information during human motion. The radar consists of a signal generator, an antenna array with three transmitters (Tx) and four receivers (Rx), a power amplifier (AMP),

a low pass filter, a mixer, and a digital signal processing (DSP) containing an analog-to-digital converter (ADC). The chirp signal sequence is transmitted by the signal generator through Tx. Chirp signal frequency increases linearly with time, which can be used to detect the moving speed of the target object. After mixing, filtering, and amplifying the radar echo signal from Rx, the IF signal is obtained. Finally, the IF signal is processed by DSP. Figure 2 shows the block diagram of the FMCW radar system.

The FMCW radar signal format can be simplified as a sawtooth modulated waveform in Fig. 3. Each chirped pulse has 100 ADC samples. The fast time sampling frequency is 20 MHz, so the LFM pulse duration $T_c = 50$ μs. In addition, the slow time sampling frequency is set to 32 Hz, so the frame period $T_a = 31.25$ ms. The transmitting signal x_T can be expressed as:

$$x_T(t) = A_T \exp\left[2\pi f_c(t) + \pi \frac{B}{T_c} t^2 + \varphi(t) \right] \quad (1)$$

where the parameters T_c and B denotes the duration and starting frequency of the chirp, A_T is the amplitude of transmitted signal, $f_c(t)$ is the frequency of transmitted chirp and $\varphi(t)$ is the phase of the signal.

Then, the radar transmitter TX emits electromagnetic waves to the human body, which are captured by the radar receiver RX after human reflection. Assume the distance between the radar and the human body is d_0, the received signal can be deduced as:

$$x_R(t) = A_R \exp\left[2\pi f_c(t - t_d) + \pi \frac{B}{T_c}(t - t_d)^2 + \varphi(t - t_d) \right] \quad (2)$$

where $A_R = a A_T$ for the amplitude of the received signal, a a scale factor, $t_d = 2d_0/c$ is the round trip delay and c is the speed of light, d_0 fixed distance from the radar to the human body, $x(t)$ is the chest wall displacement caused by respiration and heartbeat.

The transmitted signal $x_T(t)$ generated by the oscillator and the received signal $x_R(t)$ is frequency differenced through the mixer. The instantaneous frequency of the signal after the frequency difference is equal to the difference in the instantaneous frequency of the two input sine waves, and the phase is equal to the difference in the phase of the two input sine waves. Therefore, after filtering and amplification after mixing, the output baseband signal $b(t)$ can be expressed as

$$b(t) = A_b \exp\left[j\left(2\pi \frac{2Bd(t)}{cT_c} t + \frac{4\pi d_0}{\lambda} + \frac{4\pi x(t)}{\lambda} \right) \right]. \quad (3)$$

Radar measures the human chest wall's displacement to obtain the signs (breathing and heartbeat). The FMCW radar calculates the variation of the small displacement of the human chest wall by measuring the change of the phase in the distance unit with time. The motion displacement of the chest wall $x(t)$ is:
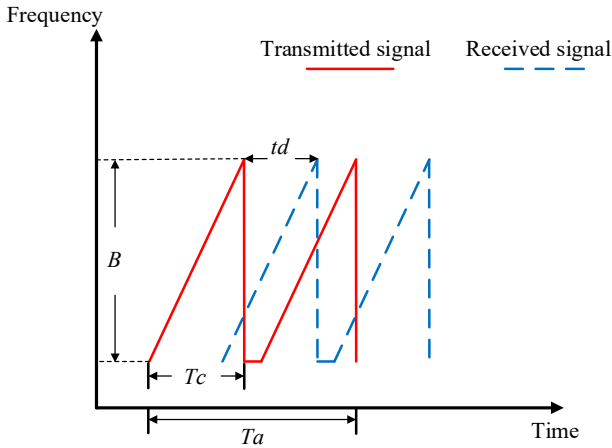
Fig. 3. FMCW signal.

$$x(t) = \text{unwrap}\left[\arctan\left(\frac{Q(t)}{I(t)}\right)\right] \quad (4)$$

where $I(t)$ and $Q(t)$ are the real part and imaginary part of the baseband signal, respectively, the real-time phase value is obtained by processing the arctangent demodulation algorithm.

2.2 Sign Extraction Based on CZT

During action recognition, CZT can locally refine and amplify the narrow-band spectrum interval of interest in the global spectrum of the breath signal and heartbeat signal, and extract accurate information of a specific frequency band. Compared with the FFT algorithm, CZT can realize the narrowband analysis of the signal and significantly improve the accuracy of estimation. The CZT flow chart is shown in Fig. 4.

Let N-point finite-length sequence x, $n = 0, 1, \ldots, N-1$, the sampling frequency is f_s, sequence interval is $[f_1, f_2]$, bandwidth $f_w = f_2 - f_1$. CZT is a finite sampling point calculated by equal angle interval sampling along a spiral circumference on a z plane.

$$Z_k = AW^{-k} = A_0 W_0 \exp\left[j(\theta_0 + k\varphi_0)\right], k = 0,1,...,M-1 \quad (5)$$

where M is the number of sampling points in the target spectrum interval, the vector radius $A = A_0 \exp(j\theta_0)$, and the phase $W = W_0 \exp(-j\varphi_0)$, A_0 and θ_0 are the vector radius and the phase of the starting sampling point z_0, φ_0 is the difference between adjacent sampling points, W_0 is the extension rate of the spiral. For N-point finite-length sequence $x(n)$, the CZT at the sampling point z_k can be expressed as
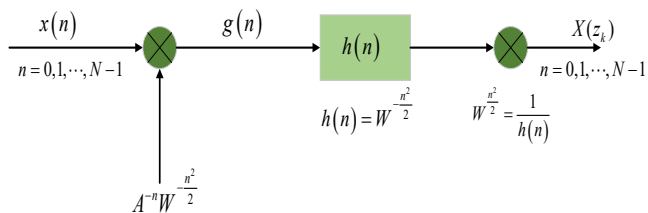
Fig. 4. CZT algorithm block diagram.

CZT Algorithm

Input: $x_h[n]$

Output: Heartbeat/Breath

1. Determination of target frequency band according to normal heart rate range during setting $[f_{min}, f_{max}]$ and sampling frequency f_s.

2. Determining the required spectral resolution based on requirements, Δf calculate the number of narrowband spectrum sampling points M, initial phase θ_0, adjacent phase φ_0:

   $M = (f_{min} - f_{max}) / \Delta f$,

   $\theta_0 = 2\pi f_{min} / f_s$,

   $\varphi_0 = 2\pi \Delta f / f_s$.

3. In order to ensure the spectrum of the signal, CZT analysis should be carried out on the circle $A_0 = W_0 = 1$, substituting the above parameters into (6), the refined spectrum of the frequency band can be calculated as

   $$X(z_k) = \sum_{n=0}^{N-1} x(n) \exp\left[-j\left(2\pi f_{min} / f_s + k \cdot 2\pi \Delta f / f_s\right)\right], k = 0,1,...,M-1.$$

4. Finding the maximum spectrum peak in target spectrum $X(z)$, the corresponding frequency is the current heart or respiration.

Fig. 5. CZT algorithm flow.

$$X(z_k) = CZT[x(n)] =$$

$$\sum_{n=0}^{N-1} x(n) z_k^{-n} = W^{\frac{k^2}{2}} \sum_{n=0}^{N-1}\left[x(n) A^{-n} W^{\frac{n^2}{2}}\right] W^{-\frac{(k-n)^2}{2}}. \quad (6)$$

Assuming $g(n) = x(n) A^{-n} W^{\frac{n^2}{2}}$, $h(n) = W^{-\frac{n^2}{2}}$, the $X(z_k)$ can be obtained

$$X(z_k) = W^{\frac{k^2}{2}}[g(k) * h(k)]. \quad (7)$$

The normal heartbeat frequency range was 0.8–2 Hz, and the respiratory frequency range was 0.1–0.5 Hz. The sufficient spectral resolution of the sign signal in this range was respectively analyzed in detail.

Figure 5 is the specific process of the CZT algorithm.

2.3 Radar Data Feature Selection

We conducted experiments to collect radar data for five operations. For comparison purposes, six features were extracted from the radar data, which can be seen in Tab. 1. In the following, the latter four are introduced in detail. N and x_i denote the number of samples and the ith radar sample, respectively, and $u(x)$ indicates a unit-step function.

(a) Wilson Amplitude (*WAMP*) is the number of times that the difference between the two consecutive amplitudes

ID	Extraction Feature	Acronym
1	Integral of Absolute Value	IAV
2	Variance	VAR
3	Wilson Amplitude	WAMP
4	Zero Crossing	ZC
5	Number of Turns	NT
6	Mean of Amplitude	MA

Tab. 1. Eigenvalues of respiratory and heartbeat signals.

exceeds a certain threshold. It can be formulated as:

$$WAMP = \sum_{i=1}^{N-1} u\left(\left|x_{i+1} - x_i\right| - T\right).$$ (8)

(b) Zero-Crossing (*ZC*) represents the number of times that the amplitude of the signal passes through zero:

$$ZC = \sum_{i=1}^{N-1} u\left(-x_i x_{i+1}\right).$$ (9)

(c) Number of Turns (*NT*) counts the number of changes in the sign of the slope, in other words, the number of signal peaks:

$$NT = \sum_{i=1}^{N-2} u\left[\left(x_{i+1} - x_i\right)\left(x_{i+1} - x_{i+2}\right)\right].$$ (10)

(d) Mean of Amplitude (*MA*): This feature determines the mean of the difference in amplitudes of two consecutive samples:

$$MA = \frac{1}{N} \sum_{i=1}^{N-1} \left|x_{i+1} - x_i\right|.$$ (11)

Owing to the use of CZT, the coefficients of each order chirp Z-transform transmit the characteristics of the motion signal. The real component, absolute value component, phase component, and imaginary component of the coefficient are extracted, and the amplitude, slope change, and zero-crossing time are provided as the input of the classifier.

2.4 Convolution Neural Network

Apart from the classifier, a CNN network is designed for classification. CNN [35] is a typical feedforward neural network, which is composed of convolutional layer, pooling layer and fully connected layer. Each level of CNN usually contains a convolutional layer and a pooling layer. Through multiple convolution and pooling alternating operations, the correlation features of input data are extracted. Finally, the fully connected layer is used to transform the feature map matrix into one-dimensional vectors and input them into the classifier to realize HMR.

The typical frame of the convolution layer contains the following.

1) Convolution layer: It performs convolution computation based on micro-Doppler data and trains amplitude, slope variation, and zero-crossing time to compute features.

$$O_{j,k}^l = \sigma\left(x_{j,k}^l\right),$$ (12)

$$l_{j,k}^l = b_{j,k}^l + W_k^l * X_i^{l-1}$$ (13)

where $\sigma(\ )$ is the activation function, $x_{j,k}^l$ is the input of the jth neuron at layer l and X_i^{l-1} is the output of the ith neuron at layer $(l-1)$, W_k^l and $b_{j,k}^l$ denote the weight vector and bias of the kth filter kernel at layer l, and $l_{j,k}^l$ denotes the ith local region at layer $(l-1)$.

2) Max pooling layer: The spatial pooling reduces the dimension of each feature map, but retains the most important information. The purpose of sub-sampling is to obtain input representation by reducing the dimension of an input representation, which helps to reduce over-fitting.

$$O_{i,k}^l = \max_{(i-1)H+1 \le j \le iH} O_{j,k}^{l-1}$$ (14)

where $O_{(\cdot),k}^{(\cdot)}$ is the feature vector for the kth filter kernel at layer $(l-1)$ and H is its height, i is the corresponding new feature vector.

3) Fully connected layer (with flatten and dense layers): Then merge several convolution layers into a fully connected layer. The goal of the fully connected layer is to flatten advanced features learned by the convolution layer. It combines all the features of the original input. The output vector O^l of the lth fully-connected layer can be described as

$$O^l = \sigma(I^l),$$ (15)

$$I^l = (W^l)^{\text{T}} O^{l-1} + b^l$$ (16)

where I^l, W^l and b^l are the input vector, weight matrix, and bias vector of the fully connected layer of layer l respectively.

4) Output layer. The output layer uses a softmax function to predict the multi-class classification as follows:

$$p_c^{(s)} = \frac{\exp(\theta_c^{\text{T}} O^{(s),L-1})}{\sum_{c=1}^{C} \exp\left(\theta_c^{\text{T}} O^{(s),L-1}\right)}$$ (17)

where L is the maximum of layer number, the superscript s denotes the sth sample, the subscript c denotes the cth class of total classification number C, $O^{(s),L-1}$ is the output vector of the previous layer, and θ_c^{T} is the weight vector for the cth class.

2.5 Efficient Channel Attention Enabled Convolutional Neural Network

Recently, the attention mechanism module has been improved to strengthen feature aggregation and the combination of channel and spatial attention. As the most potential method to improve deep CNN, the global correlation network (GCNet) combines the advantages of both Squeeze-and-Excitation Networks (SENet) and Non-Local Neural Networks (NLNet), but most NL-based attention modules are too complex to be suitable for too many convolution blocks. These methods all increase the model's complexity to improve the optimization performance. However, the ECA module requires few parameters under the premise of ensuring the performance gain, which can improve the performance of the model while preventing the model from being too complicated. The structure of ECA is shown in Fig. 6 [36].

The specific working process of the ECA module is first to perform global mean processing on the data of each
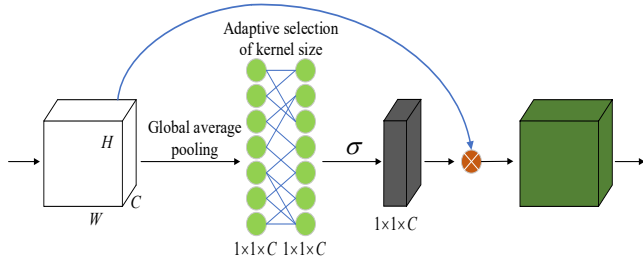
Fig. 6.   ECA structure.

channel after convolution transformation. The purpose is to obtain the global information of each channel and make up for the defect that the information outside the local perceptual field cannot be obtained when the convolution kernel is small:

$$y_c = \frac{1}{W \times H} \sum_{i=1}^{W} \sum_{j=1}^{H} u_c(i,j) \quad (18)$$

where u_c represents characteristic channel, y_c is the global eigenvalue of u_c, c is the number of feature channels, W, H represent the width and length of the data, respectively. Since the purpose of ECA is local cross-channel interaction, only interactions with K adjacent channels are considered when calculating channel weights. The expression is:

$$w_i = \sigma\left(\sum_{j=1}^{k} a^j y_i^j\right), y_i^j \in \Omega_i^k. \quad (19)$$

In the formula, Ω_i^k represents the set of k adjacent channels of y_i^j, σ is sigmoid function. This local constraint avoids the interaction of all channels in the fully connected layer and greatly improves the efficiency of the model. Each ECA module involves $k \cdot c$ parameters, which is much less than $c^2 \cdot (c/r)$ parameters in the SE module. Thus, the expression can be implemented by one-dimensional convolution of k convolution kernels:

$$w = \sigma\left(C1D_k(y)\right). \quad (20)$$

As mentioned above, k is a key parameter in the model, which solves the range size of channel interaction, so the selection of k value is a key factor affecting the performance of the model. The k value is related to the number of channels c, and there is a certain mapping relationship between

the two. Exponential functions are often used to deal with this nonlinear mapping relationship. Since the number of channels c is usually set to an integer power of 2, the following expression can be obtained:

$$c = 2^{(y \times k - b)}. \quad (21)$$

Given the number of channels c, the expression of k can be derived as:

$$k = \left(\frac{\log_2 c}{\gamma} + \frac{b}{\gamma}\right). \quad (22)$$

In the formula, γ and b are the adjustment parameters, and the value of this model k is 2.

Based on CNN, ECA is used to improve the network model. ECA-CNN includes an input layer, convolution layer, Rectified Linear Unit (ReLU), Batch Normalization (BN) layer, ECA, max pooling layer, and fully connected layer, as shown in Fig. 7. In convolution layer and pooling the BN layer is added between the layers. The ECA module is added after each BN layer. The convolution layer extracts different features of the input. ReLU increases network sparsity and reduces over-fitting. The BN layer improves training speed and reduces the risk of over-fitting. The ECA module extracts important features, and the pooling layer decreases the number of model parameters and optimizes the workload. The fully connected layer connects all features and sends the output value to the classifier for classification.

In Fig. 7, BN is located behind the convolution layer, which reduces the risk of model over-fitting, and at the same time, improves the training speed of the model. Based on normalization, the input value distribution of any neuron in each neural network is forced to normalize to a mean value of 0, the standard normal distribution with a variance of 1, so that a relatively large gradient can be obtained and the gradient can be avoided.

With the establishment of the ECA-CNN network, we collect training data by performing different types of human motion behaviors, such as shaking, marking time, standing still, jumping, and sitting-up. Storing training data and performing training is processing in a high-performance computing unit (HPC) with a GPU. Because of the streamlining of features, the network model is small, only 100 kb.
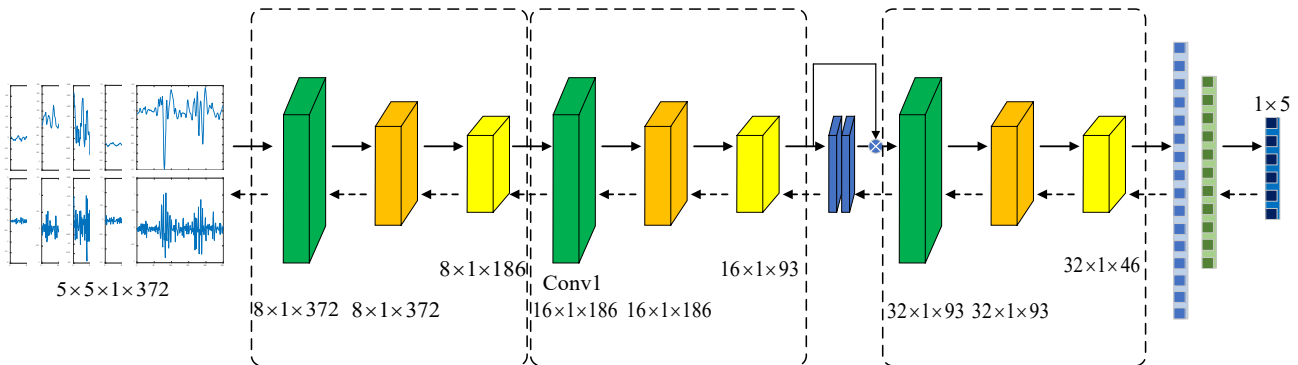
Fig. 7.   The main structure of the ECA-CNN model. Extract respiratory and heartbeat eigenvalues as inputs to the ECA-CNN model, and the final output is the action result.

3. Experimental Results and Performance Analysis

3.1 Radar Configuration and Platform

This section introduces the experimental results using different classifiers and discusses the change of classification effect caused by different input data combinations.

The experimental environment and the radar equipment selected for data acquisition are shown in Fig. 8. Millimeter-wave radar is Texas Instrument IWR1443Boost. The radar system parameters used in this paper are shown in Tab. 2. The detection accuracy can reach 20–100 μm because of the signal-to-noise ratio of the radar system is very high.

During the experiment, the radar is right in front of the human chest while shaking, standing still, and marking. In the jump experiment, the radar rises at an angle of 15–20°, sit-up data acquisition, and the radar down to 15–20° angle. The measurement range of all experimental action data is about 0.5 meter from the radar.

3.2 Experimental Data

In this article, five human actions are designed, including shaking (shake, a), marking (Mt, b), standing still (Ss, c), jumping (Jump, d), and sitting-up (sit-up, e). To verify the validity of the data, 1156 sample data for each type of human motion have been collected.

Figure 9 presents a complete action diagram and the respiratory signal diagram and the heartbeat signal diagram corresponding to each action. It should be noted that an ac-

Fig. 8. (a) is the experimental environment, (b) is IWR 1443 Boost radar and (c) is the radar measurement angle diagram.

Radar Configuration	Value
Radar Modulation	FMCW
Bandwidth B	4 GHz
Initial Form Frequency f_c	77 GHz
Fast Time Sampling Frequency f_f	2 MHz
Slow Time Sampling Frequency f_s	32 Hz
Duration T_c	50 μs
Test Distance	0.5 m–1.0 m

Tab. 2. Radar system parameter configuration.

(e)Sit-up
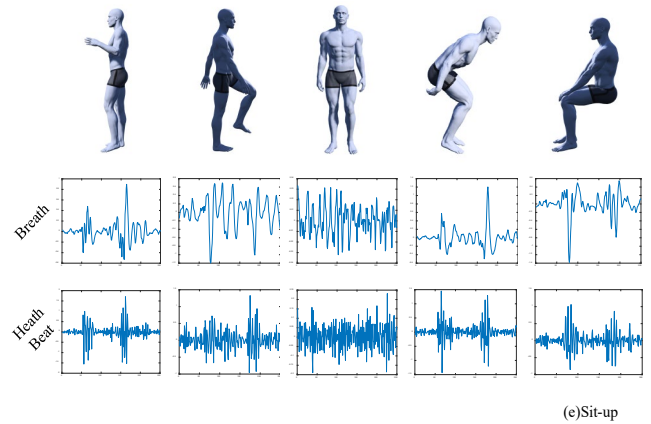
Fig. 9. Heartbeats and respiratory signals of five human motions.

tion is not completed separately, and our experiment is consistent. Figure 9 shows the results for 56 seconds. It can be seen from Fig. 9 that different human movements have different breathing and heartbeats. Figure 9(a) shows an action of shake. The action is carried out when the person stands, and the final stop position of the action is the same as the initial position. Note that each collected data sample contains multiple actions to reflect diversity.

During the experiment, when the distance between the chest wall of the human body and the radar changes, the radar echo changes. Respiration and heartbeat are the external manifestations of radar echo. In essence, they are not one-to-one correspondence.

3.3 Analysis of Human Motion Recognition Results

To study the recognition performance of human motions, first analyze the accuracy of the proposed detection methods for dwell amplitude, slope, and zero-crossing time.

In addition, this paper proposes an ECA-CNN. First, we add dimension to the data, one-hot code, label each data (real value), compare it with the predicted value, and get the error and accuracy. Then, 70% of the input data is used as the training set, and the training set is put into the network for training. Furthermore, cross-validation is carried out to divide the data set into k copies, each with $k - 1$ copies for training and one copy for verification to improve the accuracy of the network. Finally, the test set is imported into the network model to detect the accuracy of the network model.

Through 10 cycles and 3 cross-validations, the comprehensive accuracy rate reached 98.00%, and Figure 10 shows the classification result. Figure 11 shows the loss and accuracy of the ECA-CNN training set.

DT, QD, Bayesian, KNN, SVM, AlexNet, and ECA-CNN are used as different classification methods. The average accuracy of the identification is shown in Tab. 3. It can be seen from the table that the ECA-CNN method has higher recognition accuracy than other methods. The experimental results show that the classification model has encouraging advantages.
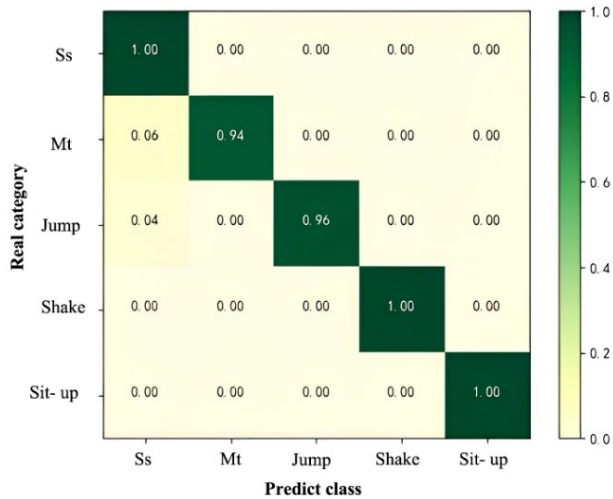
Fig. 10. Classification results of ECA-CNN.
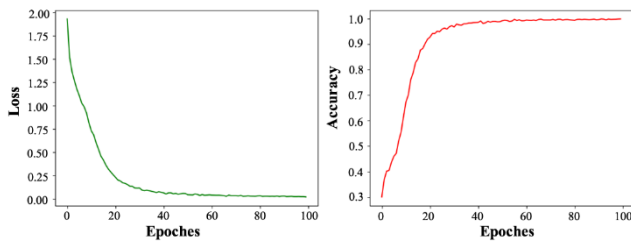
Fig. 11. Loss and accuracy results of ECA-CNN.

Methods	Human Motion Classification					Speed
	Stand still	Jump	Shake	Marking time	Sit-up	
DT	88.6%	87.6%	89.6%	86.5%	81.4%	7.3 ms
QD	89.2%	86.7%	88.7%	89.8%	83.3%	7.5 ms
Bayesian	90.3%	88.7%	89.7%	87.5%	85.4%	8.2 ms
KNN	89.9%	87.78%	88.34%	90.1%	89.8%	8.7 ms
SVM	92.1%	91.87%	92.3%	91.15%	91.8%	8.8 ms
AlexNet	72.5%	71.8%	72.8%	71.9%	69.5%	7.5 ms
ECA-CNN	100%	94.0%	96.0%	100%	99.0%	8.1 ms

Tab. 3. The average accuracy of different classifiers.

4. Conclusion

In this paper, a human motion recognition method by combining vital sign characteristic value and ECA-CNN is proposed. The six extracted features are used as the input of the ECA-CNN method, and the corresponding human motion types are used as the output of the network. Comparable with the method based on the range-Doppler map, the proposed method was accurate and calculation-less. Also, the motion recognition was qualitatively compared with the traditional methods, and differences were statistically analyzed. Experimental data showed that the proposed method's accuracy had reached 98.00% in recognizing five specific human motions, outperforming recent research. It presented an innovative technology for privacy-preserving in-home motion analysis and recognition, which created possibilities for providing seamless in-home health monitoring.

References

[1] BAO, J. B., ZHOU, L., LIU, G.H., et al. Current state of care for the elderly in China in the context of an aging population. *BioScience Trends,* 2022, vol. 16, no. 2, p. 107–118. DOI: 10.5582/bst.2022.01068

[2] ROBLEDO, L. M. G., CANO-GUTIERREZ, C., GARCIA, E. V. Healthcare for older people in Central and South America. *Age and Ageing,* 2022, vol. 51, no. 5, p. 1–4. DOI: 10.1093/ageing/afac017

[3] PIRZADA, P., WILDE, A., DOHERTY, G. H., et al. Ethics and acceptance of smart homes for older adults. *Informatics for Health and Social Care,* 2021, vol. 47, no. 1, p. 10–37. DOI: 10.1080/17538157.2021.1923500

[4] PHILIP, N. Y., RODRIGUES, J. J. P. C., WANG, H. G., et al. Internet of Things for in-home health monitoring systems: Current advances, challenges and future directions. *IEEE Journal on Selected Areas in Communications*, 2021, vol. 39, no. 2, p. 300–310. DOI: 10.1109/JSAC.2020.3042421

[5] PHAM, M., YANG, D., SHENG, W. H. A sensor fusion approach to indoor human localization based on environmental and wearable sensors. *IEEE Transactions on Automation Science and Engineering*, 2019, vol. 16, no. 1, p. 339–350. DOI: 10.1109/TASE.2018.2874487

[6] NASIRI, S., KHOSRAVANI, M. R. Progress and challenges in fabrication of wearable sensors for health monitoring. *Sensors and Actuators A: Physical*, 2020, vol. 312, p. 1–17. DOI: 10.1016/j.sna.2020.112105

[7] PENG, D. B., LIU, Y. H. Wireless sensor acquisition of human motion parameters based on blockchain. *Journal of Sensors*, 2021, p. 1–13. DOI: 10.1155/2021/4564143

[8] LIU, Z. B., HUANG, J. X., HAN, J. W., et al. Human motion tracking by multiple RGBD cameras. *IEEE Transactions on Circuits and Systems for Video Technology*, 2017, vol. 27, no. 9, p. 2014–2027. DOI: 10.1109/TCSVT.2016.2564878

[9] YAN, B. J., ZHANG, H., YAO, Y. C., et al. Heart signatures: Open-set person identification based on cardiac radar signals. *Biomedical Signal Processing and Control*, 2022, vol. 72, p. 1–12. DOI: 10.1016/j.bspc.2021.103306

[10] WANG, M. Y., ZHANG, Y. M., CUI, G. L. Human motion recognition exploiting radar with stacked recurrent neural network. *Digital Signal Processing*, 2019, vol. 87, p. 125–131. DOI: 10.1016/j.dsp.2019.01.013

[11] ZHANG, R. Y., CAO, S. Y. Real-time human motion behavior detection via CNN using mm-wave radar. *IEEE Sensors Letters,* 2019, vol. 3, no. 2, p. 1–4. DOI: 10.1109/LSENS.2018.2889060

[12] MAITRE, J., BOUCHARD, K., BERTUGLIA, C., et al. Recognizing activities of daily living from UWB radars and deep learning. *Expert Systems with Applications*, 2021, vol. 164, p. 1–13. DOI: 10.1016/J.ESWA.2020.113994

[13] SHEN, H. M., XU, C., YANG, Y. J., et al. Respiration and heartbeat rates measurement based on autocorrelation using IR-UWB radar. *IEEE Transactions on Circuits and Systems II: Express Briefs,*

2018, vol. 65, no. 10, p. 1470–1474. DOI: 10.1109/TCSII.2018.2860015

[14] GOUVEIA, C., TOME, A., BARROS, F., et al. Study on the usage feasibility of continuous-wave radar for emotion recognition. *Biomedical Signal Processing and Control*, 2020, vol. 58, p. 1–10. DOI: 10.1016/j.bspc.2019.101835

[15] YEN, H. Y., KUROSAWA, M., KIRIMOTO, T., et al. A medical radar system for non-contact vital sign monitoring and clinical performance evaluation in hospitalized older patients. *Biomedical Signal Processing and Control*, 2022, vol. 75, p. 1–12. DOI: 10.1016/j.bspc.2022.103597

[16] WU, W. H., STASZEWSKI, R. B., LONG, J. R. A 56.4-to-63.4 GHz multi-rate all-digital fractional-N PLL for FMCW radar applications in 65 nm CMOS. *IEEE Journal of Solid-State Circuits,* 2014, vol. 49, no. 5, p. 1081–1096. DOI: 10.1109/JSSC.2014.2301764

[17] VANDERSMISSEN, B., KNUDDE, N., JALALVAND, A., et al. Indoor person identification using a low-power FMCW radar. *IEEE Transactions on Geoscience and Remote Sensing*, 2018, vol. 56, no. 7, p. 3941–3952. DOI: 10.1109/TGRS.2018.2816812

[18] ALIZADEH, M., SHAKER, G., DE ALMEIDA, J. C. M., et al. Remote monitoring of human vital signs using mm-wave FMCW radar. *IEEE Access,* 2019, vol. 7, p. 54958–54968. DOI: 10.1109/ACCESS.2019.2912956

[19] DING, C. W., ZHANG, L., GU, C., et al. Non-contact human motion recognition based on UWB radar. *IEEE Journal on Emerging and Selected Topics in Circuits and Systems*, 2018, vol. 8, no. 2, p. 306–315. DOI: 10.1109/JETCAS.2018.2797313

[20] WANG, D. Y., YOO, S. W., CHO, S. H. Experimental comparison of IR-UWB radar and FMCW radar for vital signs. *Sensors*, 2020, vol. 20, p. 1–22. DOI: 10.3390/s20226695

[21] LOPES, A., NORONHA OSORIO, D. F., SILVA, H. G., et al. Equivalent pipeline processing for IR-UWB and FMCW radar comparison in vital signs monitoring applications. *IEEE Sensors Journal,* 2022, vol. 22, no. 12, p. 12028–12035. DOI: 10.1109/jsen.2022.3173218

[22] PENG, Z. Y., MUNOZ-FERRERAS, J. M., TANG, Y., et al. A portable FMCW interferometry radar with programmable low-IF architecture for localization, ISAR imaging, and vital sign tracking. *IEEE Transactions on Microwave Theory and Techniques*, 2017, vol. 65, no. 4, p. 1334–1344. DOI: 10.1109/TMTT.2016.2633352

[23] HE, M., NIAN, Y. J., GONG, Y. S. Novel signal processing method for vital sign monitoring using FMCW radar. *Biomedical Signal Processing and Control*, 2017, vol. 33, p. 335–345. DOI: 10.1016/j.bspc.2016.12.008

[24] LEE, H., KIM, B. H., PARK, J. K., et al. A novel vital-sign sensing algorithm for multiple subjects based on 24-GHz FMCW Doppler radar. *Remote Sensing,* 2019, vol. 11, no. 10, p. 1–15. DOI: 10.3390/rs11101237

[25] MERCURI, M., LU, Y. T., POLITO, S., et al. Enabling robust radar-based localization and vital signs monitoring in multipath propagation environments. *IEEE Transactions on Biomedical Engineering,* 2021, vol. 68, no. 11, p. 3228–3240. DOI: 10.1109/TBME.2021.3066876

[26] YANG, Z. T., QIU, W., SUN, H. J., et al. Robust radar emitter recognition based on the three-dimensional distribution feature and transfer learning. *Sensors*, 2016, vol. 16, no. 3, p. 1–14. DOI: 10.3390/s16030289

[27] LIU, S. K., YAN, X. P., LI, P., et al. Radar emitter recognition based on SIFT position and scale features. *IEEE Transactions on Circuits and Systems II: Express Briefs,* 2018, vol. 65, no. 12, p. 2062–2066. DOI: 10.1109/TCSII.2018.2819666

[28] SAKAMOTO, T., AUBRY, P. J., OKUMURA, S., et al. Noncontact measurement of the instantaneous heart rate in a multi-person scenario using X-band array radar and adaptive array processing.

IEEE Journal of Emerging and Selected Topics in Circuits and Systems, 2018, vol. 8, no. 2, p. 280–293. DOI: 10.1109/JETCAS.2018.2809582

[29] CHIAN, D. M., WEN, C. L., WANG, F. K., et al. Signal separation and tracking algorithm for multi-person vital signs by using Doppler radar. *IEEE Transactions on Biomedical Circuits and Systems*, 2020, vol. 14, no. 6, p. 1346–1361. DOI: 10.1109/TBCAS.2020.3029709

[30] NEEMAT, S., KRASNOV, O., YAROVOY, A. An interference mitigation technique for FMCW radar using beat-frequencies interpolation in the STFT domain. *IEEE Transactions on Microwave Theory and Techniques,* 2019, vol. 67, no. 3, p. 1207–1220. DOI: 10.1109/TMTT.2018.2881154

[31] LI, C. Z., UN, K. F., MAK, P. I., et al. Overview of recent development on wireless sensing circuits and systems for healthcare and biomedical applications. *IEEE Journal on Emerging and Selected Topics in Circuits and Systems*, 2018, vol. 8, no. 2, p. 165–177. DOI: 10.1109/JETCAS.2018.2822684

[32] KIM, Y., MOON, T. Human detection and activity classification based on micro-Doppler signatures using deep convolutional neural networks. *IEEE Geoscience and Remote Sensing Letters*, 2016, vol. 13, no. 1, p. 8–12. DOI: 10.1109/LGRS.2015.2491329

[33] EROL, B., AMIN, M. G. Radar data cube analysis for fall detection. In *IEEE International Conference on Acoustics, Speech and Signal Processing (ICASSP)*. Calgary (Canada), 2018, p. 2446–2450. DOI: 10.1109/ICASSP.2018.8461512

[34] TRAN, N., KILIC, O., NAHAR, S., et al. Contactless monitoring and classification of human motion activities by using SFCW radar. In *IEEE International Symposium on Antennas and Propagation (APSURSI)*. Fajardo (Puerto Rico, USA), 2016, p. 883–884. DOI: 10.1109/APS.2016.7696150

[35] ANWAR, S. M., MAJID, M., QAYYUM, A., et al. Medical image analysis using convolutional neural networks: A review. *Journal of Medical Systems,* 2018, vol. 42, no. 11, p. 1–13. DOI: 10.1007/s10916-018-1088-1

[36] WANG, Q. L., WU, B. G., ZHU, P. F., et al. ECA-net: Efficient channel attention for deep convolutional neural networks. In *IEEE/CVF Conference on Computer Vision and Pattern Recognition (CVPR)*. Boston (USA), 2020, p. 11531–11539. DOI: 10.1109/CVPR42600.2020.01155

About the Authors ...

Kaiyu CHEN was born in 1999. He received the Bachelor of Engineering (2021) in Automation from the Henan University, Zhengzhou, China. He is pursuing the Master of Control Science and Engineering from the Zhejiang Sci-Tech University, Hangzhou, China.

Minming GU (corresponding author) was born in 1982. He received the Bachelor of Engineer, Master of Engineering and Doctor of Engineering degrees from the Zhejiang Sci-Tech University, Hangzhou, China, in 2005, 2008, and 2018, respectively. Currently he is an Associate Professor at the Zhejiang Sci-Tech University. His research interests include radar signal analysis and real-time fault detection.

Zhixiang CHEN was born in 1999. He received the Bachelor of Engineering (2021) in Marine Electronic and Electrical Engineering from the Zhejiang Ocean University, Zhoushan, China. He is pursuing the Master of Control Science and Engineering from the Zhejiang Sci-Tech University, Hangzhou, China.